Passive wavefield imaging using the energy norm

Daniel Rocha[1], Paul Sava[1] & Jeffrey Shragge[2]
[1] *Center for Wave Phenomena, Colorado School of Mines*
[2] *Center for Energy Geoscience, the University of Western Australia*

ABSTRACT

In passive seismic monitoring, full wavefield imaging offers a robust approach for the estimation of source location and mechanism. With multicomponent data and the full anisotropic elastic wave equation, the coexistence of P- and S- modes at the source location in time-reversal modeling allows the development of imaging conditions that identify the source position and radiation pattern. We propose an imaging condition for passive wavefield imaging that is based on energy conservation and is directly related to the source mechanism. Similar to the correlation between decomposed P- and S- wavefields, which is the most common imaging condition used in passive elastic imaging, the proposed imaging condition compares the different modes present in the displacement field without costly wave-mode decomposition, and produces a strong and focused correlation at the source location. Numerical experiments demonstrate the advantages of the proposed imaging condition (compared to others that require decomposed wavefields), its sensitivity with respect to velocity inaccuracy and sparse acquisition, and its quality and efficacy in estimating the source location.

Key words: passive seismic, microseismic, imaging condition, conservation of energy, multicomponent, elastic imaging

1 INTRODUCTION

Passive seismic monitoring uses signals caused by either natural or induced seismicity to infer subsurface properties. The main difference with respect to conventional exploration seismology is the absence of a controlled source. Although the seismic source location for passive seismic is not known, one can apply methods similar to those in active seismic acquisition to achieve an image (showing the location of the source) and a proper Earth model (with information about physical properties from the subsurface) (Duncan and Eisner, 2010; Maxwell et al., 2010; Xuan and Sava, 2010; Behura et al., 2013; Blias and Grechka, 2013; Witten and Shragge, 2015; Bazargani and Snieder, 2016).

For oil and gas exploration, passive seismic monitoring is called microseismic monitoring, since this type of induced seismicity has low orders of magnitude (Warpinski et al., 2012). Microseismic monitoring has become a powerful technique for obtaining attributes from unconventional reservoirs, and its most common application is investigation of hydraulic fracturing stimulations. Fluid injection into a reservoir induces microseismic events, which can be observed by seismic monitoring either from the surface or from a borehole. Using the recorded data, one can estimate the microseismic source location, and therefore, locate where the hydraulic fracturing occurs in the subsurface (Maxwell, 2010; Michel and Tsvankin, 2013). Furthermore, the joint estimation of both source location and mechanism potentially provides information about fault and fracture orientation in the presence of multiple microseismic events (Zhebel and Eisner, 2012; Jeremic et al., 2014).

Wavefield imaging can be adapted to estimate microseismic source locations, and is usually implemented in two steps: (1) backpropagation of the recorded wavefield into an Earth model; and (2) application of an imaging condition to extract the source location and/or origin time from the extrapolated wavefield (McMechan, 1982; Gajewski and Tessmer, 2005; Xuan and Sava, 2010; Nakata and Beroza, 2016). Alternatively, for multicomponent data, one typically employs imaging procedures that exploit the different wave modes present in elastic data. The coexistence of P- and S- wavefields in space and time at the source allows for a PS imaging condition implemented in three steps: (1) backpropagation of the recorded multicomponent wavefield; (2) wave-mode decomposition of the backpropagated displacement field; and (3) zero-lag crosscorrelation of the two decomposed wavefields (P- and S- wavefields) (Artman et al., 2010; Witten and Artman, 2010; Douma and Snieder, 2015).

We propose an imaging condition for passive seismic data similar to the PS imaging condition, but without step (2): wave-mode decomposition. A well-designed imaging condi-

tion attenuates the correlation between identical wave modes in the displacement field and, at the same time, highlights the correlation of different wave modes at the source location. Based on energy conservation of elastic wavefields, we define our imaging condition that involves the kinetic and potential terms of an elastic wavefield, and these terms are computed using solely the displacement field. The proposed imaging condition is successful in forming an elastic image with attenuated artifacts for active imaging experiments, i.e. reverse time migration, as shown in previous work (Rocha et al., 2016b,c). In this paper, we explain how the same imaging condition is applicable to passive imaging, and we demonstrate its effectiveness in locating seismic sources using synthetic experiments in realistic settings.

2 THEORY

In this section, we review the elastic wave equations used in wavefield imaging and the most common imaging conditions for passive seismic imaging utilizing multicomponent data. Then, we propose an imaging condition based on the energy norm of an elastic wavefield.

2.1 Passive wavefield imaging

The elastic wave equation with no external sources is written as (Aki and Richards, 2002)

$$\rho\ddot{\mathbf{U}} = \nabla\cdot\left[\underline{\underline{\mathbf{c}}}\nabla\mathbf{U}\right] \ , \tag{1}$$

where $\mathbf{U}\left(\mathbf{x},t\right)$ is the displacement field as a function of space ($\mathbf{x}$) and time (t), $\rho(\mathbf{x})$ is the density, and $\underline{\underline{\mathbf{c}}}(\mathbf{x})$ is the 4th-order stiffness tensor. The superscript dot on the displacement field indicates time differentiation. If we assume the medium is isotropic and slowly varying, equation 1 is reduced to

$$\rho\ddot{\mathbf{U}} = \left(\lambda+2\mu\right)\nabla\left(\nabla\cdot\mathbf{U}\right) - \mu\nabla\times\left(\nabla\times\mathbf{U}\right) \ . \tag{2}$$

Equation 2 can be written as a function of velocities by substituting $V_P^2 = \frac{\lambda+2\mu}{\rho}$ and $V_S^2 = \frac{\mu}{\rho}$:

$$\ddot{\mathbf{U}} = V_P^2\nabla\left(\nabla\cdot\mathbf{U}\right) - V_S^2\nabla\times\left(\nabla\times\mathbf{U}\right) \ , \tag{3}$$

where V_P and V_S are the P- and S-wave velocities, respectively. Using the multicomponent data recorded at the receivers, the displacement field $\mathbf{U}$ can be extrapolated in the subsurface by using either the wave equation 1 or 3 depending on the assumptions about the medium anisotropy.

Different imaging conditions that use the displacement field directly have been proposed to estimate the source location in passive wavefield imaging (Steiner et al., 2008; Jeremic et al., 2015). For instance, Steiner et al. (2008) propose to use the absolute value of the particle velocity, i.e. the time derivative of the displacement vector field. Alternatively, one can implement wave-mode decomposition, i.e. decompose the displacement field into wavefields that represent P- and S-wavefields. For isotropic media, wave-mode decomposition is typically implemented using Helmholtz decomposition (Dellinger and Etgen, 1990; Yan and Sava, 2009):

$$P = \nabla\cdot\mathbf{U} \ , \tag{4}$$

$$\mathbf{S} = \nabla\times\mathbf{U} \ , \tag{5}$$

where $P\left(\mathbf{x},t\right)$ is a scalar wavefield containing the compressional wave mode, and $\mathbf{S}\left(\mathbf{x},t\right)$ is a vector wavefield containing the transverse wave mode. For anisotropic media, wave-mode decomposition is implemented by solving the Christoffel equation (Dellinger and Etgen, 1990); however, this method demands robust techniques with significant additional cost (Yan and Sava, 2009, 2011; Cheng and Fomel, 2013).

Because the S-wavefield is a vector field, passive imaging conditions can use the energy densities E_P and E_S of the decomposed wavefields (Morse and Feshback, 1953):

$$E_P\left(\mathbf{x},t\right) = \left(\lambda+2\mu\right)\left\|\nabla\cdot\mathbf{U}\right\| \ , \tag{6}$$

$$E_S\left(\mathbf{x},t\right) = \mu\left\|\nabla\times\mathbf{U}\right\| \ . \tag{7}$$

Separated wave modes and their energy densities allow one to implement the following imaging conditions:

$$I_{PP}\left(\mathbf{x}\right) = \sum_t P\left(\mathbf{x},t\right)P\left(\mathbf{x},t\right) \equiv \sum_t E_P^2\left(\mathbf{x},t\right) \ , \tag{8}$$

$$I_{SS}\left(\mathbf{x}\right) = \sum_t \mathbf{S}\left(\mathbf{x},t\right)\cdot\mathbf{S}\left(\mathbf{x},t\right) \equiv \sum_t E_S^2\left(\mathbf{x},t\right) \ . \tag{9}$$

Notice that these imaging conditions consist of an autocorrelation of a given wave mode. A recurrent problem with autocorrelation imaging conditions is that the correlation of the wavefield with itself produces low-wavenumber content along the path where the waves propagate, e.g. between the source in the subsurface and the receivers on the surface or in a borehole.

Alternatively, one can use the different modes of the displacement field to define an imaging condition free of low-wavenumber artifacts from autocorrelation. Figure 1 illustrates how different modes interact in passive wavefield imaging. A microseismic or earthquake source generates both P- and S-waves that propagate through the subsurface (Figures 1(a) and 1(b)). For a non-scattering medium, P- and S-waves propagate at different speeds and only coexist in space and time at the source (Figures 1(c) and 1(d)). Exploiting this fact, one can define a PS imaging condition (Yan and Sava, 2008; Artman et al., 2010):

$$\mathbf{I}_{PS}\left(\mathbf{x}\right) = \sum_t P\left(\mathbf{x},t\right)\mathbf{S}\left(\mathbf{x},t\right) \ , \tag{10}$$

where $\mathbf{I}_{PS}\left(\mathbf{x}\right)$ is a multicomponent image, whose individual components represent the correlation between $P\left(\mathbf{x},t\right)$ and the corresponding component from $\mathbf{S}\left(\mathbf{x},t\right)$. In a 3-D experiment, three images can be potentially computed instead of a single one that concisely shows the source location.

In contrast, the energy norm (Rocha et al., 2016a,c) allows one to define a pair of imaging conditions for elastic reverse time migration (ERTM), where one of the imaging conditions concisely exhibits the reflectors in the subsurface. For an anisotropic medium, this pair of imaging conditions is de-

fined as (Rocha et al., 2016b)

$$I_E(\mathbf{x}) = \sum_t \left[\rho\dot{\mathbf{U}}\cdot\dot{\mathbf{V}} + \left(\underline{\underline{\mathbf{c}}}\nabla\mathbf{U}\right) : \nabla\mathbf{V}\right], \quad (11)$$

$$I_E(\mathbf{x}) = \sum_t \left[\rho\dot{\mathbf{U}}\cdot\dot{\mathbf{V}} - \left(\underline{\underline{\mathbf{c}}}\nabla\mathbf{U}\right) : \nabla\mathbf{V}\right], \quad (12)$$

where $\mathbf{U}(\mathbf{x},t)$ and $\mathbf{V}(\mathbf{x},t)$ are the source and receiver wavefields, and the symbol : indicates the Frobenius product (Appendix A). The imaging condition in equation 12 attenuates events from source and receiver wavefields with the same polarization and propagation direction. The correlation between these events contaminates the conventional images with low-wavenumber artifacts. Therefore, the imaging condition in equation 12 suppresses artifacts and delivers a single image with highlighted reflectors.

For passive imaging, in which only one wavefield is extrapolated, we can also define a pair of autocorrelation imaging conditions:

$$I_E(\mathbf{x}) = \sum_t \left[\rho\dot{\mathbf{U}}\cdot\dot{\mathbf{U}} + \left(\underline{\underline{\mathbf{c}}}\nabla\mathbf{U}\right) : \nabla\mathbf{U}\right], \quad (13)$$

$$I_E(\mathbf{x}) = \sum_t \left[\rho\dot{\mathbf{U}}\cdot\dot{\mathbf{U}} - \left(\underline{\underline{\mathbf{c}}}\nabla\mathbf{U}\right) : \nabla\mathbf{U}\right]. \quad (14)$$

For these imaging conditions, the individual terms have a special meaning in terms of energy of the elastic wavefield. The first and second terms in equations 13 and 14 represent the kinetic and potential energies of the wavefield, respectively. Therefore, equation 13 is related to the Hamiltonian operator, which measures the total energy of the wavefield, and equation 14 is related to the Lagrangian operator, which is expressed as the difference between kinetic and potential energy terms (Ben-Menahem and Singh, 1981).

Although the imaging condition in equation 14 involves autocorrelation of the displacement field $\mathbf{U}$, the correlation between the same wave modes is attenuated as shown by Rocha et al. (2016b,c). In contrast, at the source, the correlation between P- and S- modes is preserved and is directly related to the source mechanism (Appendix B). Therefore, the energy imaging condition for passive imaging correlates P- and S- wave modes using the displacement field directly, without wave-mode decomposition. For isotropic media, the costs of the PS imaging condition (equation 10) and the energy imaging condition (equation 14) are comparable, since in both cases one needs to compute wavefield derivatives; and for anisotropic media, computing equation 14 is significantly cheaper than decomposing wave modes during extrapolation, as explained earlier.

2.2 Extended imaging conditions

The imaging conditions shown previously, which consist of zero-lag correlation between wavefields, can be considered as special cases of a more general comparison between wavefields. Extending the wavefield correlation beyond zero lag provides additional information such as velocity accuracy (Sava and Vasconcelos, 2011). The temporal and spatial dependences of the wavefields allow one to compute space-lag image gathers (Rickett and Sava, 2002) and/or time-lag image gathers (Sava and Fomel, 2006). Extended imaging conditions are also applicable to passive imaging as shown by Witten and Shragge (2015) for scalar extrapolated wavefields. Therefore, for wave-mode decomposed elastic wavefields, we can define

$$I_{\alpha_1\alpha_2}(\mathbf{x},\boldsymbol{\lambda},\tau) = \sum_t \alpha_1(\mathbf{x}+\boldsymbol{\lambda},t+\tau)\,\alpha_2(\mathbf{x}-\boldsymbol{\lambda},t-\tau), \quad (15)$$

where $\boldsymbol{\lambda}$ and τ are the spatial and temporal lags, respectively. The symbols α_1 and α_2 stand for either $P(\mathbf{x},t)$ or components of $\mathbf{S}(\mathbf{x},t)$ from equation 10, creating many possible extended images for elastic potentials. Analogously, for the energy imaging condition in equations 13 and 14, we define

$$I_E(\mathbf{x},\boldsymbol{\lambda},\tau) = \sum_t \Big[\left(\rho^{1/2}\dot{\mathbf{U}}(\mathbf{x}+\boldsymbol{\lambda},t+\tau)\right)\cdot\left(\rho^{1/2}\dot{\mathbf{U}}(\mathbf{x}-\boldsymbol{\lambda},t-\tau)\right) \pm\left(\underline{\underline{\mathbf{c}}}^{1/2}\nabla\mathbf{U}(\mathbf{x}+\boldsymbol{\lambda},t+\tau)\right):\left(\underline{\underline{\mathbf{c}}}^{1/2}\nabla\mathbf{U}(\mathbf{x}-\boldsymbol{\lambda},t-\tau)\right)\Big], \quad (16)$$

where the superscript $1/2$ on the stiffness tensor simply indicates that the stiffness matrix is decomposed into its square root matrix, which multiplied by itself leads back to the original tensor. Since the stiffness tensor is positive definite, the square-root tensor $\underline{\underline{\mathbf{c}}}^{1/2}$ is uniquely determined (Shao and Lu, 2009).

In general, one can estimate the velocity inaccuracy on extended image gathers by evaluating their focusing at zero-lag. The more focused the energy is, the closer the migration velocity is to the true velocity, as shown in many cases for active source seismic wavefield tomography (Albertin et al., 2005; Yang and Sava, 2011; Diaz et al., 2013; Yang et al., 2013; Yang and Sava, 2015). In this paper, we investigate the extended images for both PS and energy imaging conditions in order to infer potential applications on velocity estimation.

3 EXAMPLES

Using simple numerical experiments, we explain how the energy imaging condition generates an image showing the source position with the correct velocity. Then, we analyze the imprint of velocity inaccuracy on conventional and extended images. Finally, we show the benefits of the energy imaging condition in a more complex synthetic model with typical acquisition configuration.

3.1 Focusing with correct velocity

Ideally, an imaging condition for passive seismic should deliver a strong and focused correlation at the source location if true model parameters are used. Figure 2(a) shows an ideal 2-D passive experiment where multicomponent receivers surround the source from all possible angles. The source mechanism consists of a stress field generated by a fault displacement oriented at 45° with respect to the horizontal. Figures 2(b) and 2(c) show the images obtained when using the autocorrelation

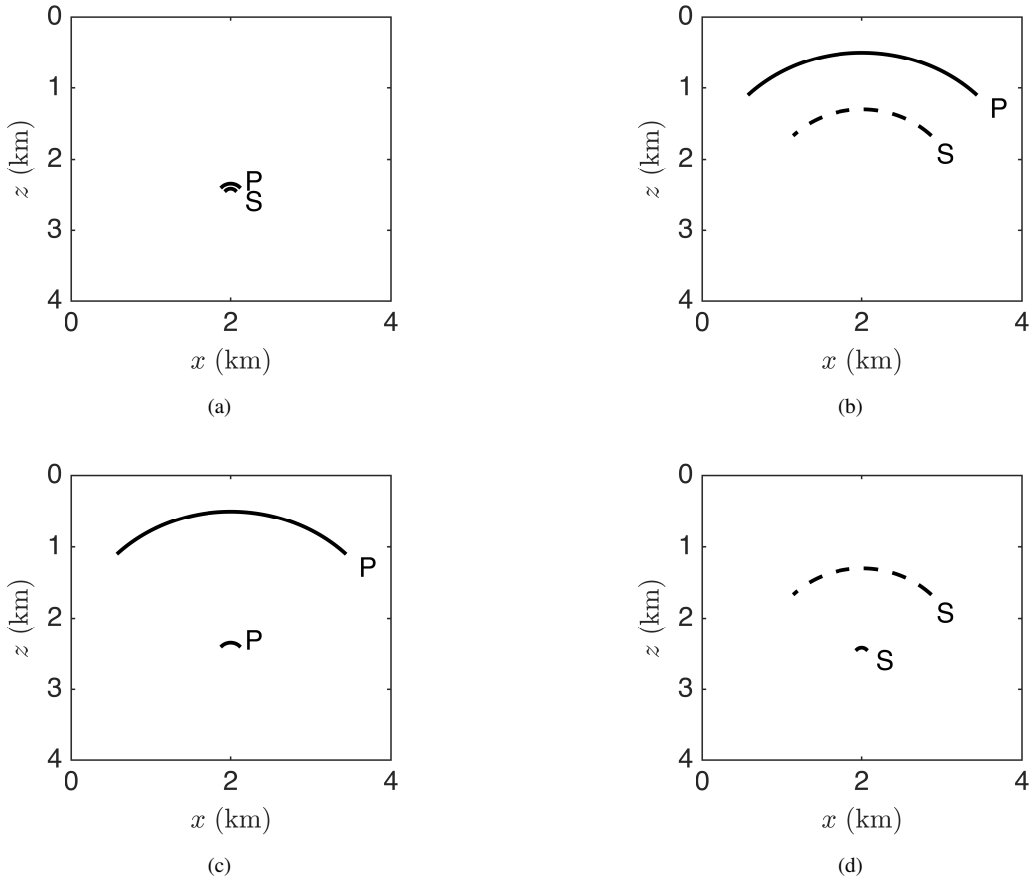


Figure 1. Schematic representation of (a) a seismic source that generates both P- (solid) and S- (dashed) waves, and (b) the propagation of these waves with different velocities in the subsurface. Due to these different propagation velocities, extrapolated P- (c) and S- (d) wavefields coexist in space and time only at the source location.

of the P- and S-wavefields, respectively. The low-wavenumber content due to the autocorrelation of these wavefields prevents a better focusing at the source. Alternatively, the correlation of P- and S-wave modes generates the image in Figure 2(d) with less low-wavenumber content. The energy imaging condition based on the Hamiltonian operator (Figure 2(e)) represents the total energy stacked over time, resulting in a strong correlation at the source location along with a similar low-wavenumber pattern. In contrast, the energy imaging condition based on the Lagrangian operator (Figure 2(f)) results in a zero-amplitude correlation away from the source, and a strong and focused correlation at the source location. The image pattern in Figure 2(f) contains the signature of the source function as shown in Figure 3. The source function is a 20 Hz Ricker wavelet (Figure 3(a)), and the trace taken from the image in (Figure 3(b)) has a similar waveform compared to the source function.

The experiment depicted in Figure 2 is not feasible in the real world. Figures 4(a) and 5(a) show a similar experiment geometry but with a dense and a sparse array of receivers only at the surface, respectively. The low-wavenumber patterns are more prominent in the autocorrelation images in Figures 4 and 5 compared to the images in Figure 2. In particular, the PS (Figures 4(d) and 5(d)) and energy images (Figures 4(f) and 5(f)) have similar resolution and quality with the same acquisition limitations. In addition, Figures 4 and 5 show that one should consider smearing and truncation artifacts when estimating a source location using wavefield imaging methods for passive seismic, since acquired data always record an incomplete wavefield, which prevents the extrapolated waves from collapsing into a focal point.

Figure 6 shows the effect of the source mechanism on PS and energy imaging conditions. For sources describing fault or fracture planes at steep angles (Figures 6(b)-6(c) and Figures 6(b)-6(c)), both imaging conditions show smearing along their source orientation. For a horizontal source, the energy image exhibits better focusing compared to the PS image. The analysis of radiation patterns for different source orientations is important because it can help us infer the fault slip or fracture direction.

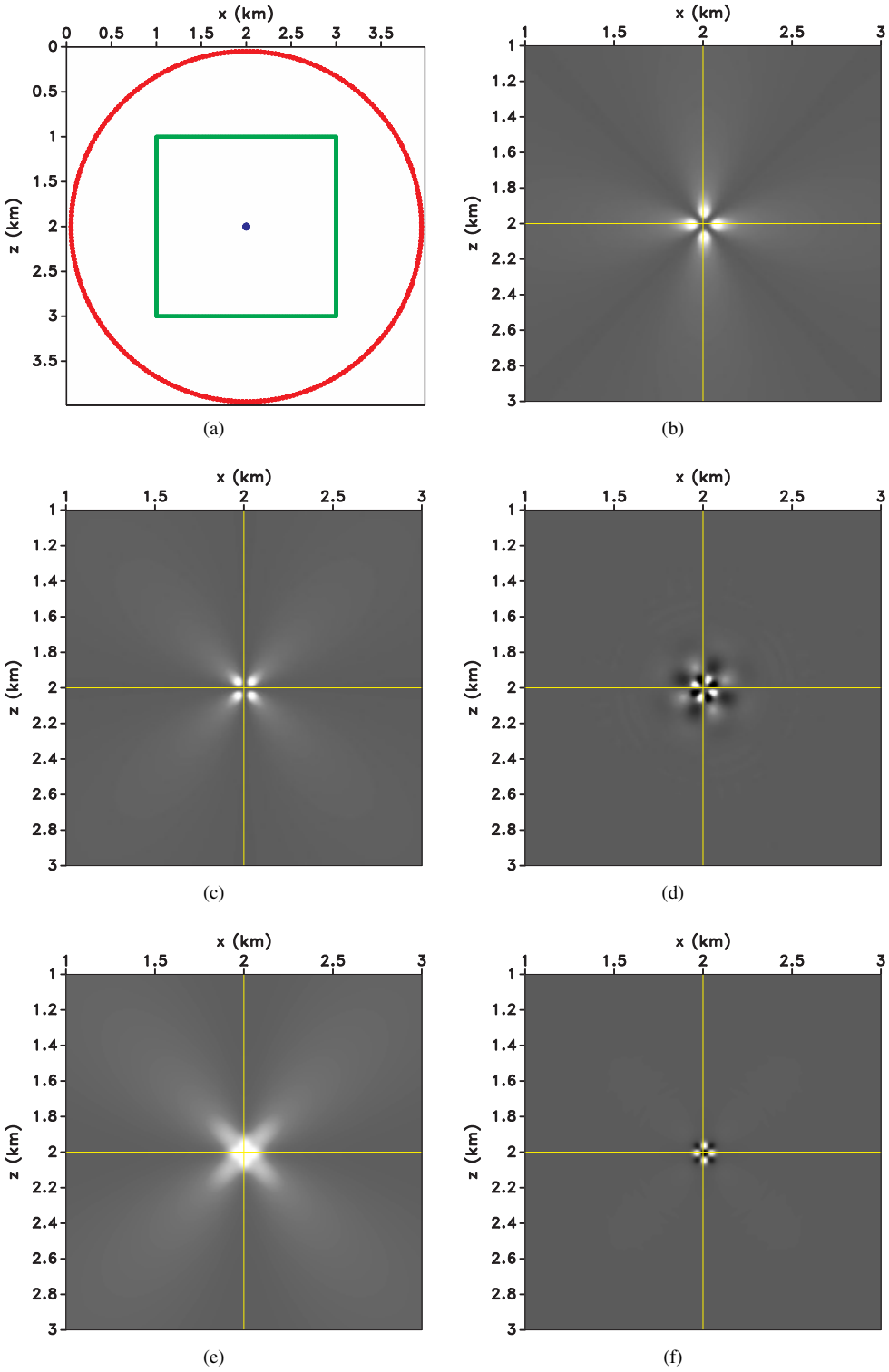
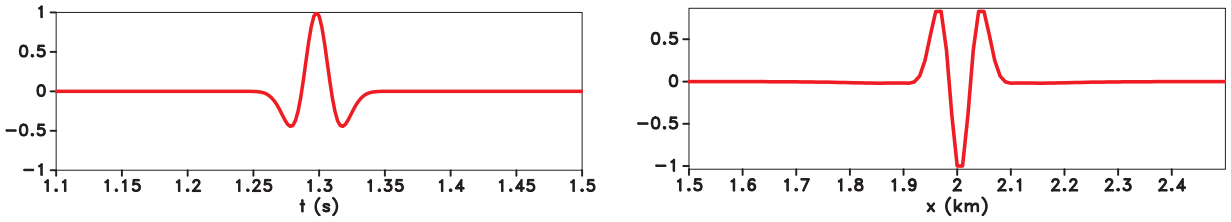


Figure 2. Ideal acquisition with equal coverage from all angles. (a) Multicomponent receivers in the circle, stress source oriented by 45° at the center, and zoom area represented by the box. (b) PP image, (c) SS image, (d) PS image, and energy images using equation 13 (e) and equation 14 (f). The image in (f) has a strong and focused peak at the source location compared to the other images.



(a) (b)

Figure 3. (a) Ricker wavelet used in the experiment in Figure 2. (b) Trace from the image in Figure 2(f) at $x = 2$ km. Notice that the image pattern in Figure 2(f) recovers the source function.

3.2 Sensitivity to changes in velocity and extended images

Assuming that the velocity used in the wavefield extrapolation is incorrect, the correlation between P- and S-waves occurs at a different location and time than for the true source. Figure 7 illustrates how a change in velocity shifts the point where P- and S- waves interact in space and time. For a source triggered at $t = 0$, Figures 7(a) and 7(b) show the correlation between P- and S- waves for the circular acquisition (Figure 2) and for the surface acquistion (Figure 4). For the surface acquisition, when the wrong P- and S- velocities are such that the correlation occurs at an earlier time, the correlation is misplaced to greater depths (Figure 7(d)). If this correlation occurs at a later time, it is misplaced to shallower depths (Figure 7(f)). However, for the circular acquisition, two correlations occur instead of one (Figure 7(c) and 7(e)).

We compute PS and energy conventional and extended images for different velocities. Figure 8 shows PS images for the circular acquisition experiment in Figure 2. The images are unfocused for the wrong velocity and show a different correlation point (Figures 8(a) and 8(c)). The correlation in Figure 8(a) is related to the case described in Figure 7(c), and Figure 8(c) is related to Figure 7(e). Due to the large number of dimensions, extended images can be computed for a fixed point (x, z) on the 2-D conventional image and are called common image point gathers (Sava and Vasconcelos, 2011), which form 3-D volumes with axes λ_x, λ_z and τ (Figures 8(d)-8(f)). In 3-D, common image point (CIP) gathers form 4-D volumes with axes $\lambda_x, \lambda_y, \lambda_z$ and τ. These CIP gathers are computed at the point where P- and S- waves correlate (points on Figures 8(a)-8(c)). Only the CIP gather with the correct velocity shows focused energy at zero lag, which is similar to the conventional and extended images for active-source imaging. However, the extended images for the wrong velocities exhibit more unfocused energy (Figures 9(d) and 9(f)).

For a more realistic acquisition, conventional images for both imaging conditions also exhibit strong correlation away from the true location (Figures 10 and 11). The vertical shift of the P- and S- wave correlation points is explained in Figures 7(d) and 7(f). Due to the more limited aperture, the extended images are less sensitive to the change in velocity (Figures 10(d)-10(f) and Figures 11(d)-11(f)). In addition, the acquisition truncation at the surface and the symmetry of the experiment create an additional low-wavenumber artifact along the propagation path (Figures 11(a) and 11(c)).

3.3 Marmousi II experiment

We illustrate our method with part of the Marmousi II model (Martin et al., 2002) in order to simulate more realistic passive acquisition in an area subject to hydraulic fracturing (Figure 12). The experiment consists of a microseismic source represented by a fracture oriented at 30° and induced by hydraulic fracturing activity in a nearby borehole (Figure 12(a)). An array of multicomponent receivers is placed inside the borehole with 80m of receiver spacing, and another denser array of receivers is placed on the surface with 40m of receiver spacing. The combination of surface and borehole arrays improves passive seismic results due to the larger effective acquisition aperture (Thornton and Duncan, 2012). The Marmousi II model contains P- and S- wave velocities (Figure 12(b)) that are not proportional to each other, i.e., the model has a spatially variable velocity ratio (V_P/V_S) (Figure 12(c)). We smooth the velocities to obtain only P- and S- direct arrivals in the synthetic data, which are shown in Figure 13. To simulate a wrong imaging velocity, we further smooth the velocities and apply a 2% decrease (Figure 12(d)).

Figure 14 shows wavefield snapshots for the P- and S-wavefields, and for PS and energy zero-lag correlations, when using the correct velocity. The snapshots are taken when the waves are close to focusing time. Artifacts due to the sparse receivers and to the data injection (creating non-physical modes) are strong but more prominent at shallow depths (less than 1 km). The energy correlation around the source location (Figure 14(h)) is visibly stronger than the surrounding artifacts and the PS correlation (Figure 14(f)).

Figure 15 shows the application of the PS and energy imaging conditions when using the correct velocity. Comparing Figures 15(a) and 15(c), note that the PS correlation is weak compared to the amplitude of the artifacts, while the energy correlation is stronger at the source location compared to the surrounding artifacts. Comparing the zoomed images (Figures 15(b) and 15(d)), note that the energy image has a more focused correlation at the source location than at the PS image. In Figure 15(d), the smearing in the source correlation compared to radiation patterns in Figures 6(e) and 6(f) potentially infers that the source mechanism is due to an oblique

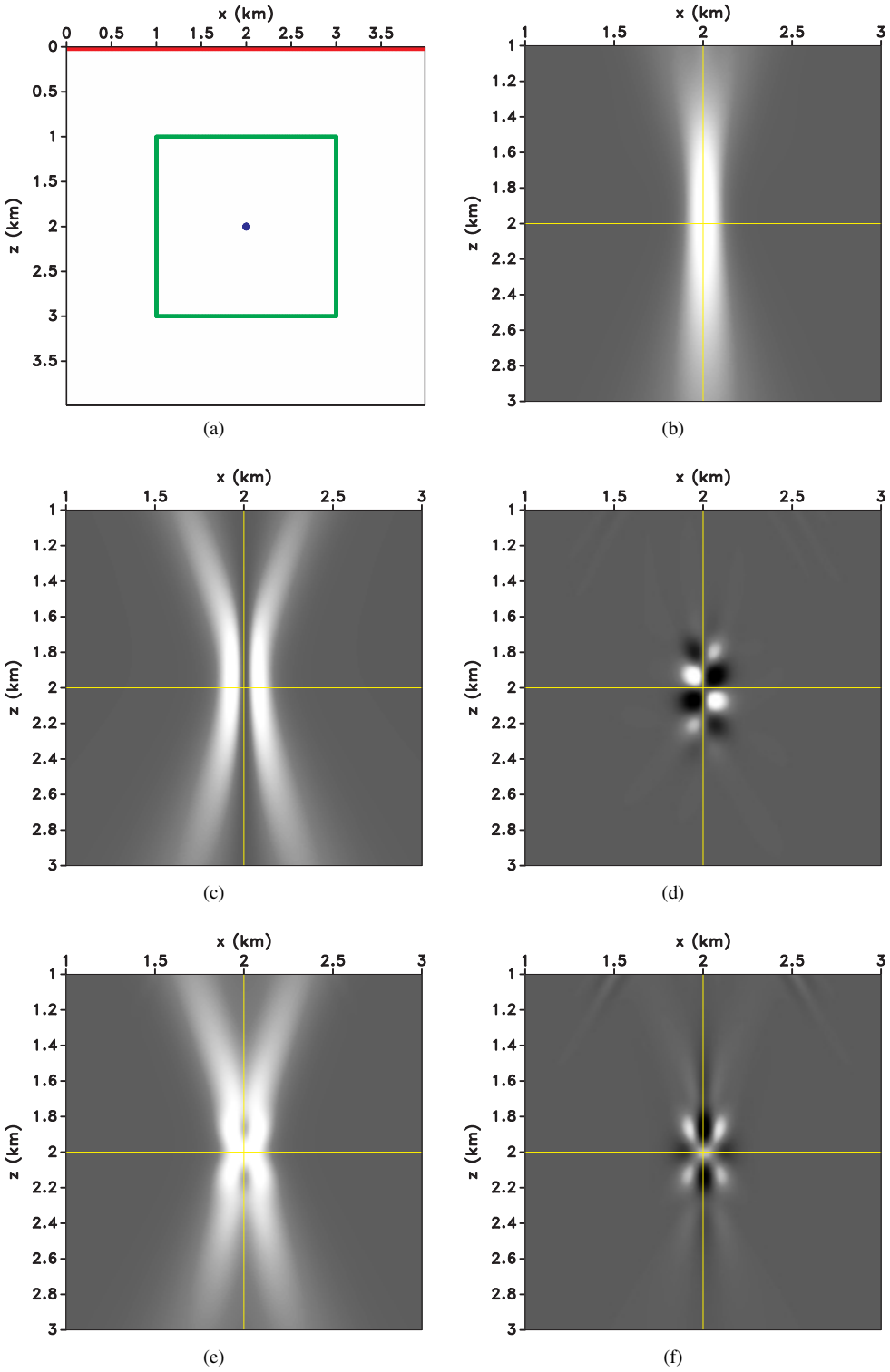


Figure 4. An acquisition with complete surface coverage. (a) Multicomponent receivers at the surface, stress source oriented by 45° at the center, and zoom area represented by the box. (b) PP image, (c) SS image, (d) PS image, and energy images using equation 13 (e) and equation 14 (f). Due to acquisition aperture, all images show vertical smearing compared to the images in Figure 2.

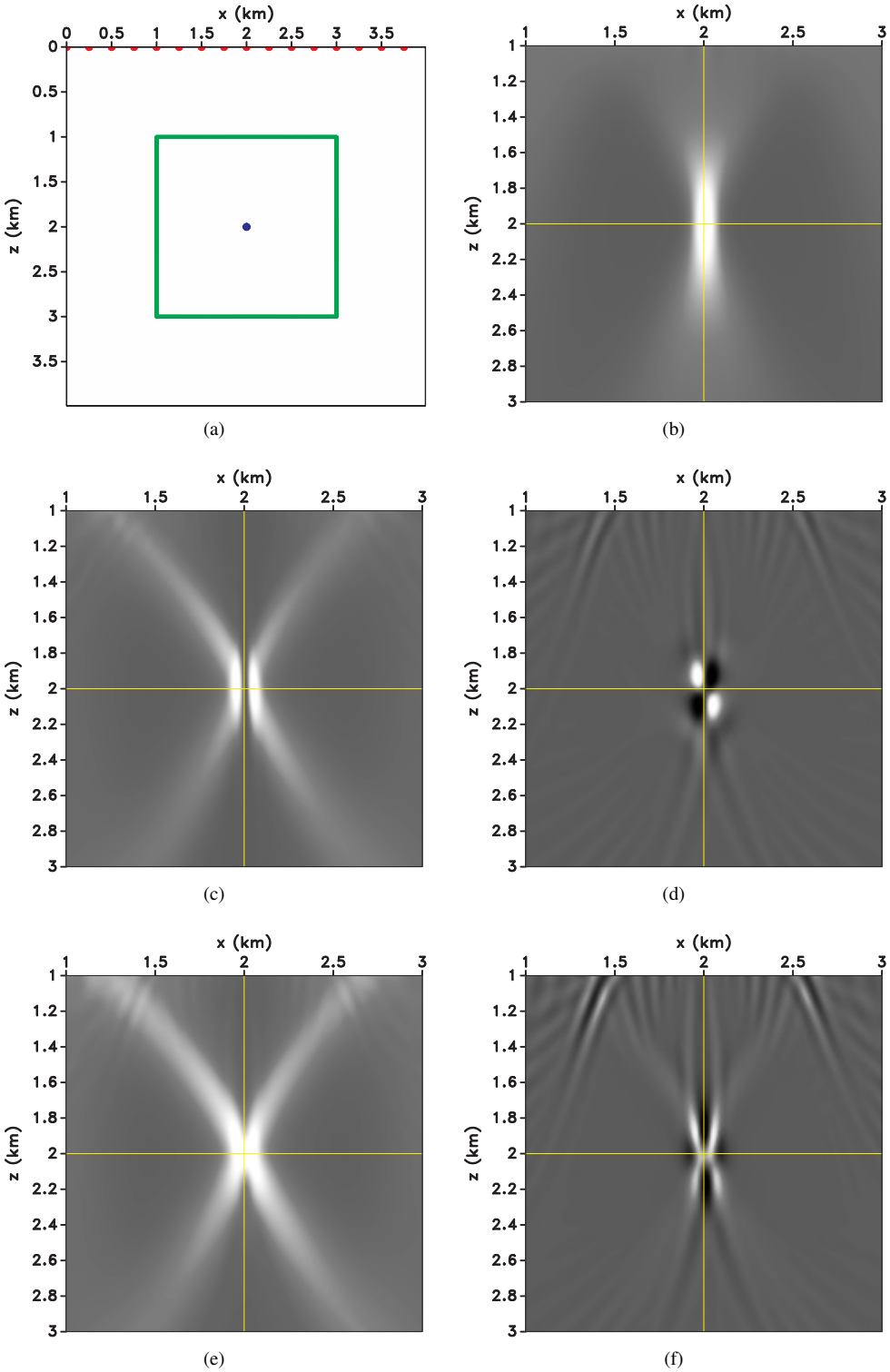


Figure 5. A more realistic acquisition with sparse surface coverage (250m spacing). (a) Multicomponent receivers at the surface, stress source oriented by 45° at the center, and zoom area represented by the box. (b) PP image, (c) SS image, (d) PS image, and energy images using equation 13 (e) and equation 14 (f). Due to the sparse receivers, all images show truncation artifacts compared to the images in Figure 4.

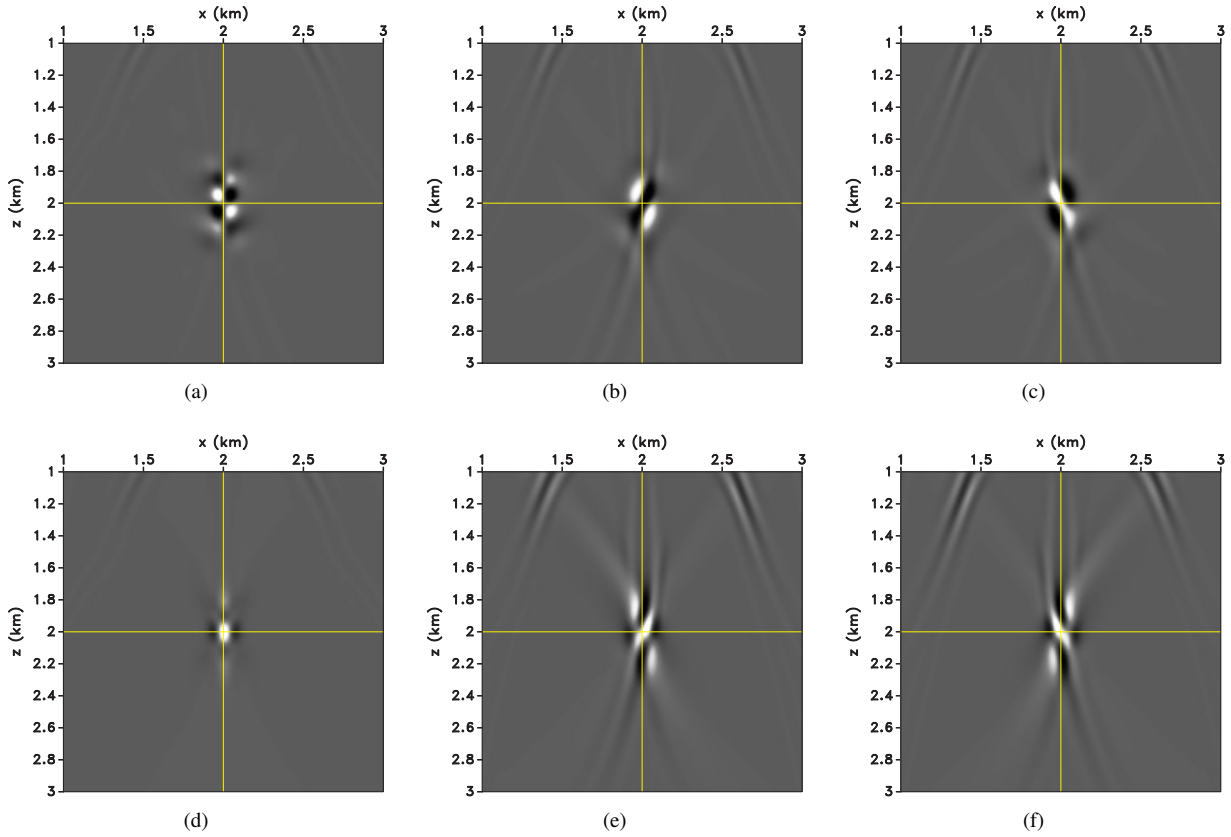


Figure 6. Images illustrating different radiation patterns for the acquisition with complete surface coverage. PS images for a stress source oriented at (a) 0°, (b) 30°, and (c) 60°. Energy images for a stress source oriented at (d) 0°, (e) 30°, and (f) 60°. Both PS and energy imaging condition have analogous radiation patterns, with exception to 0°.

fracture, which is true since the simulated stress source is oriented at 30°. With the wrong velocity (Figure 16), the artifacts are increased and both images present an unfocused correlation (Figure 16(b) and 16(d)).

The Marmousi II experiment demonstrates that the direct correlation between decomposed P- and S- wavefields produces strong imaging artifacts that surpass in amplitude the correlation at the source. The energy imaging condition involves an indirect correlation of P- and S- waves that produces a stronger correlation at the source location compared to the imaging artifacts. The difference between these two imaging conditions becomes more evident with this more complex model compared to the simple experiments shown earlier.

4 CONCLUSIONS

For passive wavefield imaging with multicomponent data, the energy imaging condition offers an elegant solution to locate seismic sources for an arbitrary Earth model. In contrast, the PS imaging condition requires a costly decomposition of the wavefields in Earth models that incorporate anisotropy. Based on the energy conservation for extrapolated wavefields, our imaging condition represents the temporal integral of the Lagrangian operator (which is the difference between kinetic and potential terms from the wavefield) and produces an image that is directly related to the source mechanism. We demonstrate for simple models that the energy and PS imaging conditions are comparable in terms of image quality, velocity sensitivity, and characterization of radiation patterns. For more realistic settings, we show that the energy imaging condition handles imaging artifacts and source focusing better than its conventional PS counterpart. Future work involves exploring the cost and further benefits of the energy imaging condition for anisotropic media, and developing a velocity inversion procedure using the unfocused energy on extended image gathers.

5 ACKNOWLEDGMENTS

We thank the sponsors of the Center for Wave Phenomena, whose support made this research possible. We acknowledge Paul Fowler and Roel Snieder for helpful discussions, and Yuting Duan for sharing her wavefield modeling codes. The reproducible numeric examples in this paper use the Madagas-

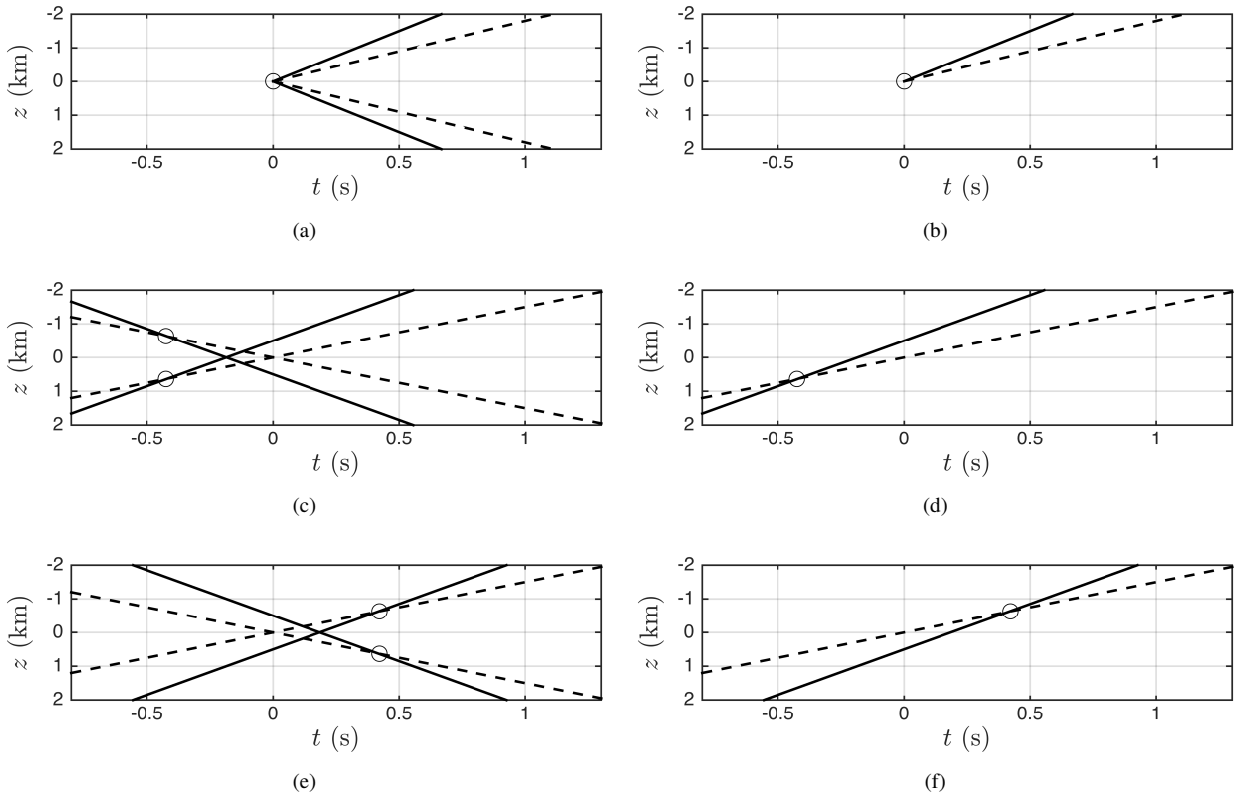


Figure 7. Schematic representation of P- (solid) and S- (dashed) wavefields correlation for wrong velocities. Circular (a), i.e., waves backpropagated from the top and bottom of the schematic model, and surface (b) acquisitions using the correct velocities. When the velocities are wrong, correlations occur at earlier/later times for circular acquisition (c)/(e), and for surface acquisition (d)/(f).

car open-source software package (Fomel et al., 2013) freely available from http://www.ahay.org.

REFERENCES

Aki, K., and P. G. Richards, 2002, Quantitative seismology, 2nd ed.: University Science Books.

Albertin, U., P. Sava, J. Etgen, and M. Maharramov, 2005, Adjoint wave-equation velocity analysis: Presented at the 76th Annual International Meeting.

Artman, B., I. Podladtchikov, and B. Witten, 2010, Source location using time-reverse imaging: Geophysical Prospecting, **58**, 861–873.

Bazargani, F., and R. Snieder, 2016, Optimal source imaging in elastic media: Geophysical Journal International, **204**, 1134–1147.

Behura, J., F. Forghani, and F. Bazargani, 2013, Improving microseismic imaging: role of acquisition, velocity model, and imaging condition: Presented at the SEG Houston 2013 Annual Meeting.

Ben-Menahem, A., and S. J. Singh, 1981, Seismic waves and sources, 1st ed.: Springer-Verlag.

Blias, E., and V. Grechka, 2013, Analytic solutions to the joint estimation of microseismic event locations and effective velocity model: Geophysics, **78**, KS51–KS61.

Cheng, J., and S. Fomel, 2013, Fast algorithms for elastic-wave-mode separation and vector decomposition using low-rank approximation for anisotropic media: Presented at the SEG Houston 2013 Annual Meeting.

Dellinger, J., and J. Etgen, 1990, Wave-field separation in two-dimensional anisotropic media: Geophysics, **55**, 914–919.

Diaz, E., P. Sava, and T. Yang, 2013, Data-domain and image-domain wavefield tomography: The Leading Edge, **32**, 1064–1072.

Douma, J., and R. Snieder, 2015, Focusing of elastic waves for microseismic imaging: Geophysical Journal International, **200**, 390–401.

Duncan, P., and L. Eisner, 2010, Reservoir characterization using surface microseismic monitoring: Geophysics, **75**, A139–A146.

Fomel, S., P. Sava, I. Vlad, Y. Liu, and V. Bashkardin, 2013, Madagascar: open-source software project for multidimensional data analysis and reproducible computational experiments: Journal of Open Research Software, **1**.

Gajewski, D., and E. Tessmer, 2005, Reverse modelling for seismic event characterization: Geophysical Journal Inter-

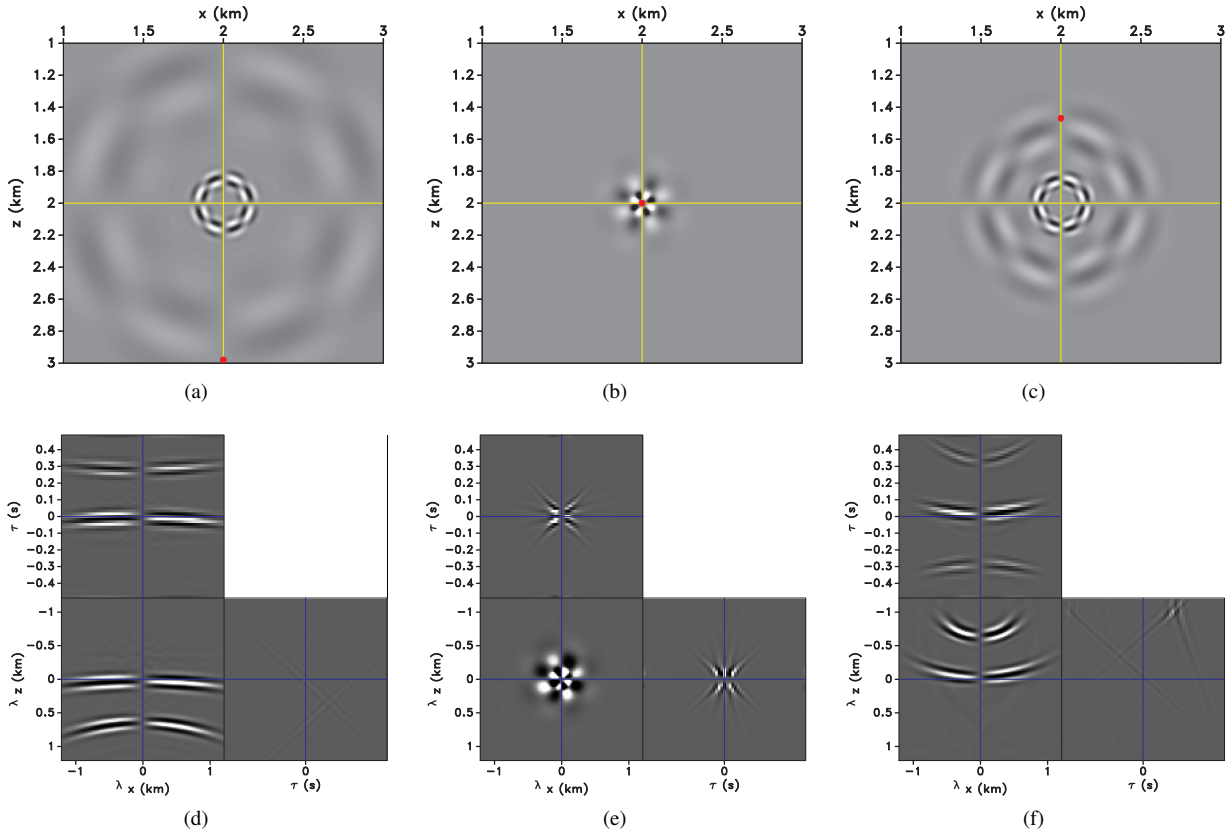


Figure 8. Velocity sensitivity of the PS imaging condition for the circular acquisition (Figure 2). Conventional/extended images for (a)/(d) 81% of the true $\frac{V_P}{V_S}$, (b)/(e) true $\frac{V_P}{V_S}$, and (c)/(f) 122% of the true $\frac{V_P}{V_S}$. Points on the conventional images indicate where the extended image are computed.

national, **163**, 276–284.

Golub, G. H., and C. F. V. Loan, 1996, Chapter 2 - Matrix Analysis, *in* Matrix computations, 3 ed.: John Hopkins University Press.

Jeremic, A., J. Kurpan, M. Thornton, and P. Duncan, 2015, Passive seismic multicomponent imaging using geometrical optics theory: Presented at the SEG New Orleans 2015 Annual Meeting.

Jeremic, A., J. Kurpan, M. Thornton, and M. Mueller, 2014, Extending passive seismic imaging to account for source mechanism effects: Presented at the SEG Denver 2014 Annual Meeting.

Lanczos, C., 1970, The variational principles of mechanics, 4th ed.: Donver Publications, **1**.

Martin, G., K. Marfurt, and S. Larsen, 2002, Marmousi-2, an updated model for the investigation of avo in structurally complex areas: Presented at the 2002 SEG Annual Meeting.

Maxwell, S., 2010, Microseismic: Growth born from success: The Leading Edge, **29**, 338–343.

Maxwell, S., J. Rutledge, R. Jones, and M. Fehler, 2010, Petroleum reservoir characterization using downhole microseismic monitoring: Geophysics, **75**, A129–A137.

McMechan, G. A., 1982, Determination of source parameters by wavefield extrapolation: Geophysical Journal International, **71**, 613–628.

Michel, O. J., and I. Tsvankin, 2013, Gradient computation for full-waveform inversion of microseismic data in vti media: Presented at the SEG Houston 2013 Annual Meeting.

Morse, P., and H. Feshback, 1953, Methods of Theoretical Physics, 1st ed.: McGraw-Hill.

Nakata, N., and G. C. Beroza, 2016, Reverse time migration for microseismic sources using the geometric mean as an imaging condition: Geophysics, **81**, KS51–KS60.

Rickett, J., and P. Sava, 2002, Offset and angle-domain common image-point gathers for shot-profile migration: Geophysics, **67**, 883–889.

Rocha, D., N. Tanushev, and P. Sava, 2016a, Acoustic wavefield imaging using the energy norm: Geophysics (accepted for publication).

———, 2016b, Anisotropic elastic wavefield imaging using the energy norm: Presented at the 78th EAGE Conference and Exhibition.

———, 2016c, Elastic wavefield imaging using the energy norm: Geophysics (accepted for publication).

Sava, P., and S. Fomel, 2006, Time-shift imaging condition in seismic migration: Geophysics, **71**, S209–S217.

Sava, P., and I. Vasconcelos, 2011, Extended imaging condition for wave-equation migration: Geophysical Prospecting,

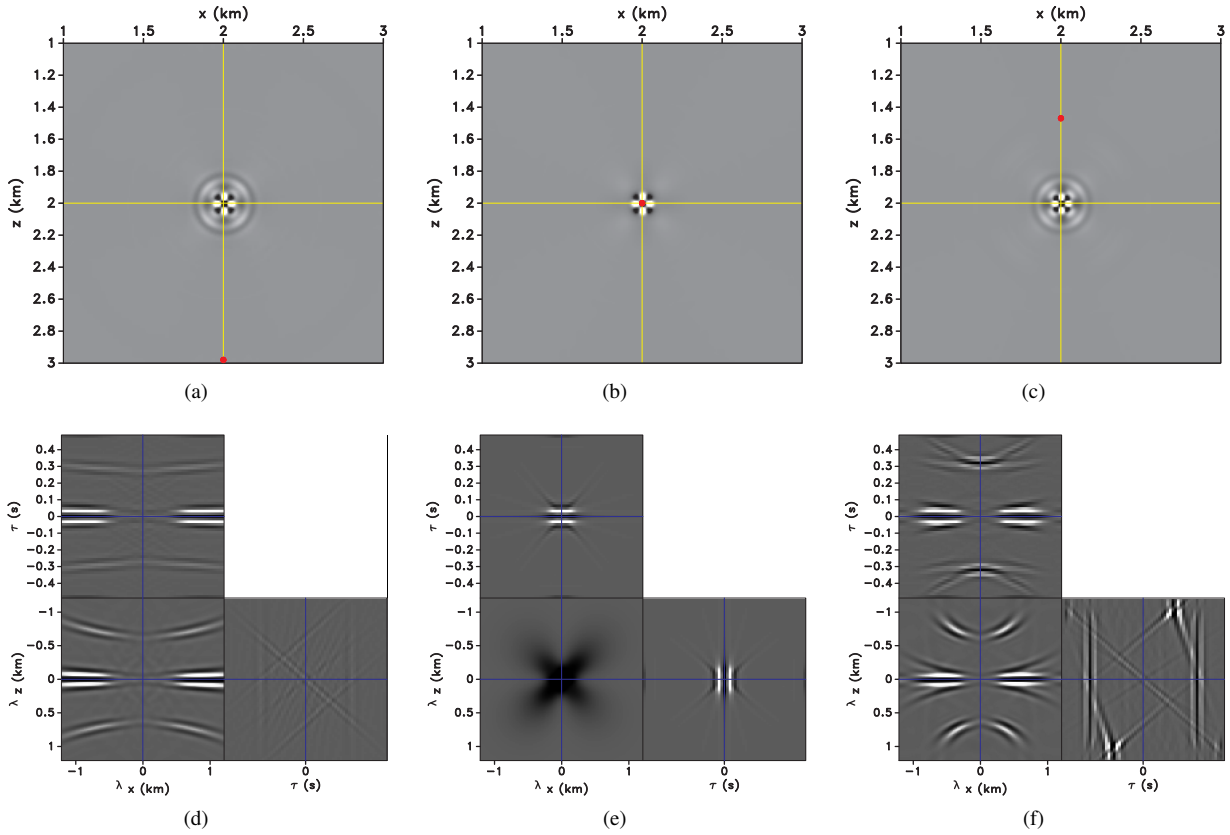


Figure 9. Velocity sensitivity of the energy imaging condition for the circular acquisition (Figure 2). Conventional/extended images for (a)/(d) 81% of the true $\frac{V_P}{V_S}$, (b)/(e) true $\frac{V_P}{V_S}$, and (c)/(f) 122% of the true $\frac{V_P}{V_S}$. Points on the conventional images indicate where the extended image are computed.

59, 35–55.

Shao, Y., and C. Lu, 2009, A direct proof of uniqueness of square-root of a positive semi-definite tensor: Applied Mathematics and Mechanics, **30**, 713–716.

Slawinski, M. A., 2003, Seismic waves and rays in elastic media, 1st ed.: Elsevier Science, **34**.

Steiner, B., E. H. Saenger, and S. M. Schmalholz, 2008, Time reverse modeling of low-frequency microtremors: Application to hydrocarbon reservoir localization: Geophysical Research Letters, **35**, L03307.

Thornton, M., and P. Duncan, 2012, Microseismic imaging with combined surface and downhole arrays: Presented at the SEG Las Vegas 2012 Annual Meeting.

Warpinski, N., J. Du, and U. Zimmer, 2012, Measurements of hydraulic-fracture-induced seismicity in gas shales: Presented at the SPE Hydraulic Fracturing Technology Conference.

Witten, B., and B. Artman, 2010, Signal-to-noise estimates of time-reverse images: Presented at the SEG Denver 2010 Annual Meeting.

Witten, B., and J. Shragge, 2015, Extended wave-equation imaging conditions for passive seismic data: Geophysics, **80**, WC61–WC72.

Xuan, R., and P. Sava, 2010, Probabilistic microearthquake location for reservoir monitoring: Geophysics, **75**, MA9–MA26.

Yan, J., and P. Sava, 2008, Isotropic angle-domain elastic reverse-time migration: Geophysics, **73**, S229–S239.

———, 2009, Elastic wave-mode separation for VTI media: Geophysics, **74**, WB19–WB32.

———, 2011, Elastic wave-mode separation for tilted transverse isotropy media: Geophysical Prospecting, **60**, 29–48.

Yang, T., and P. Sava, 2011, Wave-equation migration velocity analysis with time-lag imaging: Geophysical Prospecting, **59**, 635–650.

———, 2015, Image-domain wavefield tomography with extended common-image-point gathers: Geophysical Prospecting, **63**, 1086–1096.

Yang, T., J. Shragge, and P. Sava, 2013, Illumination compensation for image-domain wavefield tomography: Geophysics, **78**, U65–U76.

Yu, Y.-Y., 1964, Generalized Hamilton's Principle and Variational Equation of Motion in Nonlinear Elasticity Theory, with Application to Plate Theory: The Journal of the Acoustic Society of America, **36**, 111–120.

Zhebel, O., and L. Eisner, 2012, Simultaneous microseis-

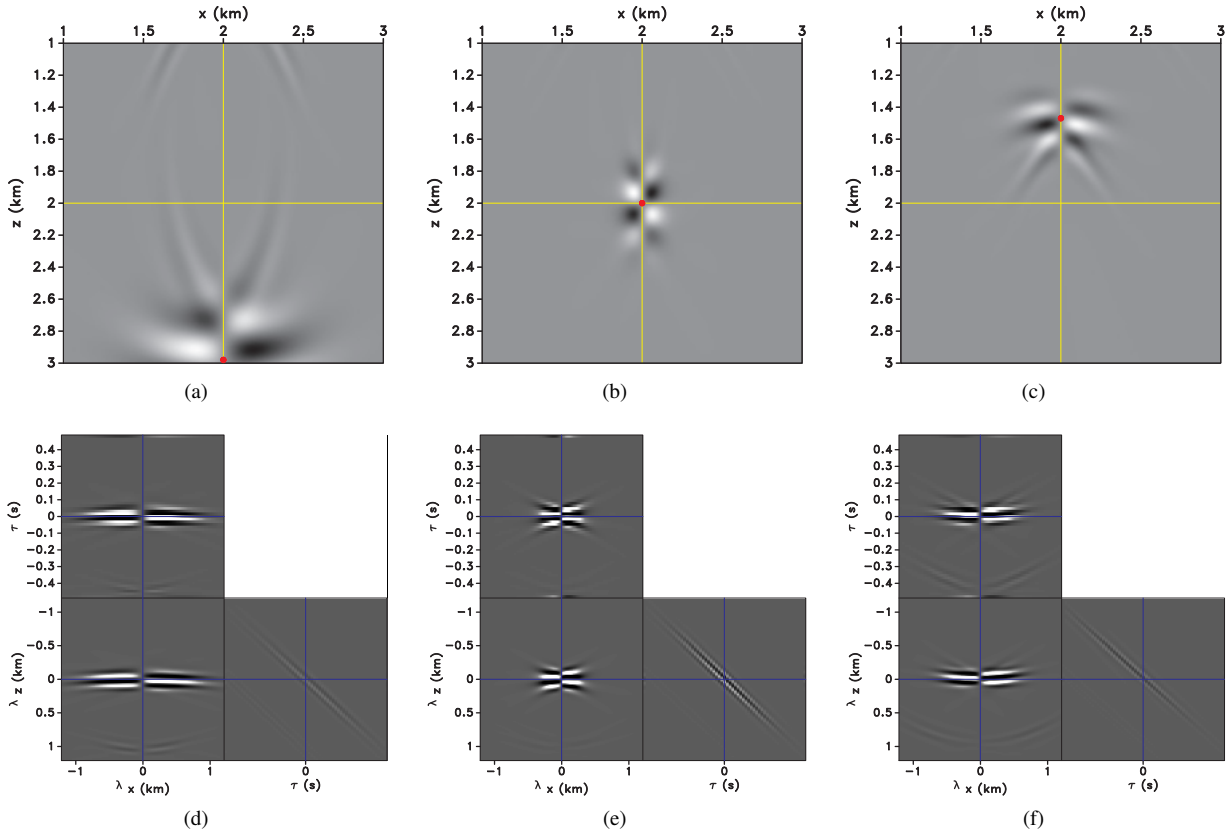


Figure 10. Velocity sensitivity of the PS imaging condition for the surface acquisition (Figure 2). Conventional/extended images for (a)/(d) 81% of the true $\frac{V_P}{V_S}$, (b)/(e) true $\frac{V_P}{V_S}$, and (c)/(f) 122% of the true $\frac{V_P}{V_S}$. Points on the conventional images indicate where the extended image are computed.

mic event localization and source mechanism determination: Presented at the SEG Las Vegas 2012 Annual Meeting.

Appendix A

Frobenius product and norm

The Frobenius norm is the most common matrix norm in numerical linear algebra. Consider an arbitrary matrix $A_{m,n}$, this norm is defined as (Golub and Loan, 1996)

$$||A||_F = \sqrt{\sum_{i=1}^{M}\sum_{j=1}^{N}|a_{ij}|^2}\ . \tag{A.1}$$

We can also define a norm of a tensor field using the inner product of associate matrices. Given tensor fields A and B, we can define the Frobenius product:

$$< A, B >_F = A : B = \sum_{i=1}^{M}\sum_{j=1}^{N} a_{ij}b_{ij}\ , \tag{A.2}$$

where M and N are the dimensions of the tensors A and B. This product can also be written in matrix form as

$$< A, B >_F = A : B = \mathrm{Tr}(A^{\mathrm{T}}B) = \mathrm{Tr}(AB^{\mathrm{T}})\ . \tag{A.3}$$

Then, we can write the Frobenius norm:

$$||A||_F = \sqrt{\mathrm{Tr}(AA^{\mathrm{T}})}\ , \tag{A.4}$$

Appendix B

Hamilton's Principle

Considering a displacement field $\mathbf{U}(\mathbf{x}, t)$, the Lagrangian density function is (Ben-Menahem and Singh, 1981)

$$\mathcal{L}(\mathbf{U}, \mathbf{x}, t) = \frac{1}{2}\rho\|\dot{\mathbf{U}}\|^2 - \frac{1}{2}\left(\underline{\underline{\mathbf{c}}}\nabla\mathbf{U}\right) : \nabla\mathbf{U}\ . \tag{B.1}$$

The first and second terms in the Lagrangian function represent the kinetic and potential energies of the wavefield, respectively. In a medium with no external forces, the action is defined as the Lagrangian density function integrated over time

$$A(\mathbf{U}) = \int_0^T \mathcal{L}(\mathbf{U}, t)\, dt\ . \tag{B.2}$$

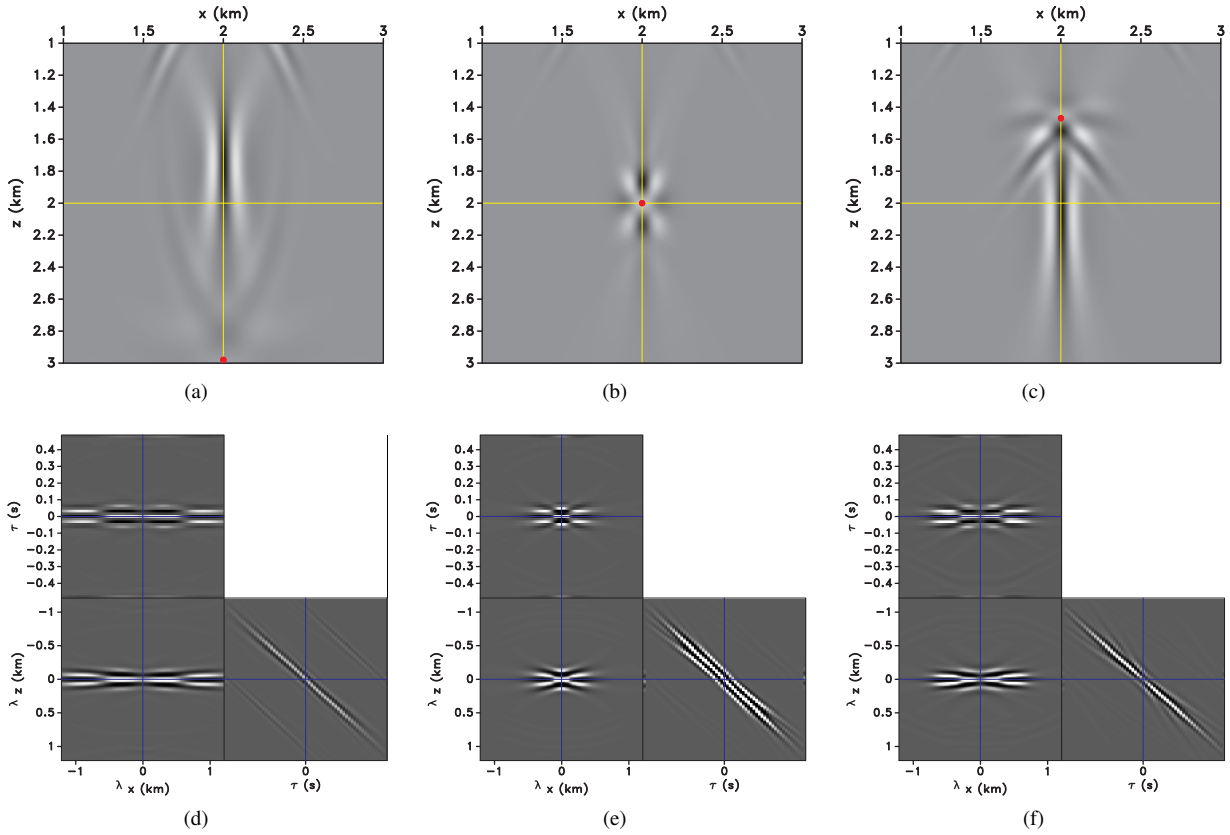


Figure 11. Velocity sensitivity of the energy imaging condition for the surface acquisition (Figure 2). Conventional/extended images for (a)/(d) 81% of the true $\frac{V_P}{V_S}$, (b)/(e) true $\frac{V_P}{V_S}$, and (c)/(f) 122% of the true $\frac{V_P}{V_S}$. Points on the conventional images indicate where the extended image are computed.

The Hamilton's variational principle states that the action is stationary under small displacements. This principle can be expressed as (Slawinski, 2003):

$$\delta A\left(\mathbf{U},\mathbf{x}\right) = \delta \int_0^T \mathcal{L}\left(\mathbf{U},t\right) dt = 0\ , \tag{B.3}$$

where δ indicates the variation of a function. The variation is permutable with a definite integral and can be defined with respect to the displacement variable (Lanczos, 1970). Hence

$$\begin{aligned}\delta A\left(\mathbf{U},\mathbf{x}\right) &= \int_0^T \delta\mathcal{L}\left(\mathbf{U},t\right) dt \\ &= \int_0^T \left[\mathcal{L}\left(\mathbf{U}+\delta\mathbf{U},t\right) - \mathcal{L}\left(\mathbf{U},t\right)\right] dt = 0\end{aligned} \tag{B.4}$$

where $\delta\mathbf{U}\left(\mathbf{x},t\right)$ is a small displacement, which satisfies $\delta\mathbf{U}(\mathbf{x},t=0) = \delta\mathbf{U}(\mathbf{x},t=T) = 0$.

We can characterize the Lagrangian $\mathcal{L}\left(\mathbf{U},t\right)$ for a particle at rest from $t=0$ to $t=T$, i.e., $\mathbf{U}=0$, for $0 \leq t \leq T$. We can consider the displacement field acting on this particular point as a small perturbance to the particle at the rest. Therefore,

$$\delta A\left(\mathbf{U},\mathbf{x}\right) = \int_0^T \mathcal{L}\left(\delta\mathbf{U},t\right) dt = 0\ . \tag{B.5}$$

This implies that, in the absence of external work from sources and considering the displacement field small, the energy imaging condition defined as the integral of the Lagrangian density function is zero.

In a volume V that contains sources, the action is defined as (Yu, 1964):

$$A\left(\mathbf{U},\mathbf{x}\right) = \int_0^T \int_V \left[\mathcal{L}\left(\mathbf{U},t\right) dV + W\right] dt\ . \tag{B.6}$$

where the external work W is

$$W = \int_V \rho\mathbf{F}\cdot\mathbf{U} dV + \int_S \left(\underline{\mathbf{t}}\cdot\mathbf{U}\right)\cdot\mathbf{n} dS\ , \tag{B.7}$$

where $\mathbf{F}\left(\mathbf{x},t\right)$ and $\underline{\mathbf{t}}\left(\mathbf{x},t\right)$ represent a body force and an external stress field acting on the surface of the considered volume, respectively. Applying the variation operator on equation B.7 and using the divergence theorem, we obtain

$$\delta W = \int_V \left[\rho\mathbf{F}\cdot\delta\mathbf{U} + \nabla\cdot\left(\underline{\mathbf{t}}\cdot\delta\mathbf{U}\right)\right] dV\ . \tag{B.8}$$

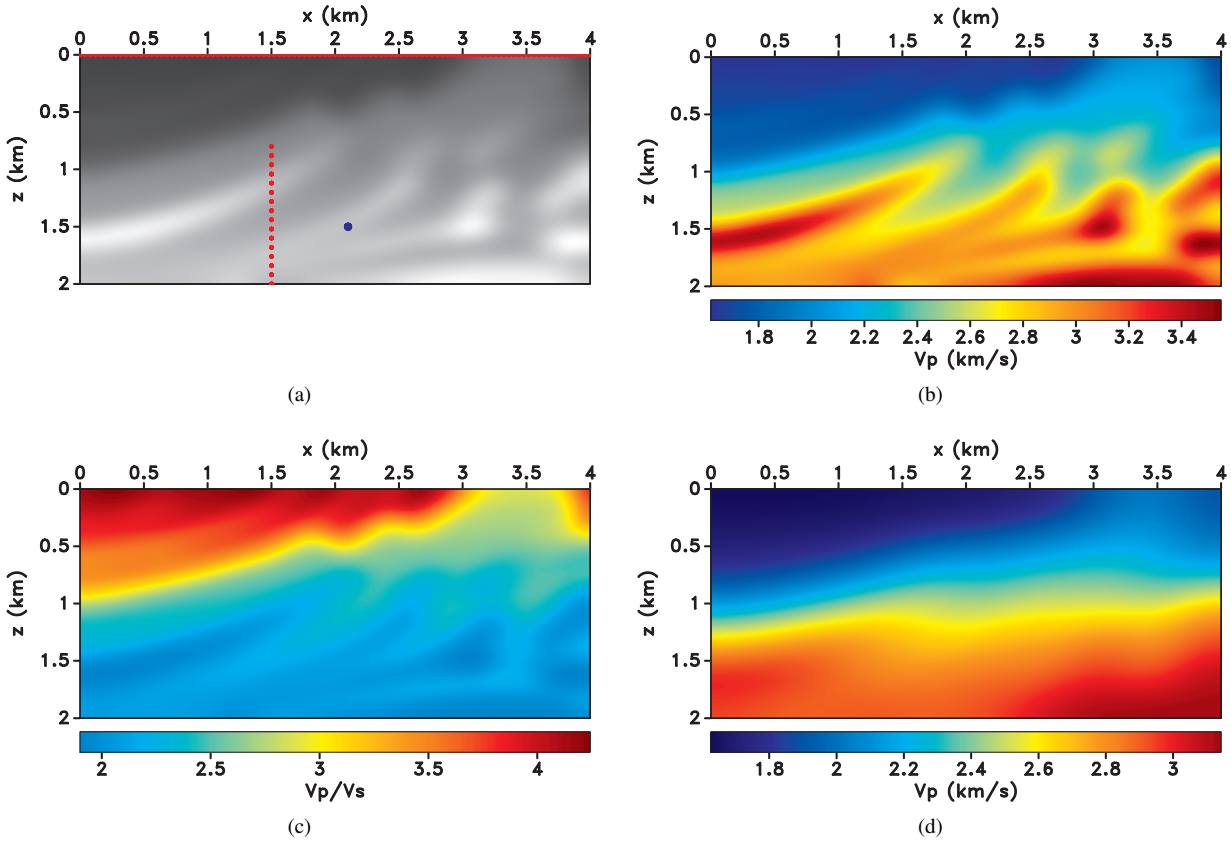


Figure 12. Acquisition geometry for the Marmousi-II experiment (a) with receivers in red and the source in blue color. (b) True P- velocity, (c) true PS velocity ratio, and (d) wrong P- velocity.

Applying the variation operator on equation B.6 and using equation B.8 leads to

$$\delta A\left(\mathbf{U}\right)=\int_0^T\int_V\left[\mathcal{L}\left(\delta\mathbf{U},t\right)+\rho\mathbf{F}\cdot\delta\mathbf{U}+\nabla\cdot(\underline{\mathbf{t}}\cdot\delta\mathbf{U})\right]dVdt=0. \tag{B.9}$$

Consider a sufficient small volume such that it contains only one discrete point. In a point where either a displacement or a stress source exists, Equation B.9 suggests that the energy imaging condition (defined as the integral of the Lagrangian density function) is equivalent to the action of existing sources

$$I_{EN}\left(\mathbf{x}\right)=\int_0^T\mathcal{L}\left(\delta\mathbf{U},t\right)dt=-\int_0^T\rho\mathbf{F}\cdot\delta\mathbf{U}+\nabla\cdot(\underline{\mathbf{t}}\cdot\delta\mathbf{U})\,dt\ . \tag{B.10}$$

The energy imaging, for waves generated by a displacement point force, becomes

$$I_{EN}\left(\mathbf{x}\right)=\int_0^T\mathcal{L}\left(\delta\mathbf{U},t\right)dt=-\int_0^T\rho\mathbf{F}\cdot\delta\mathbf{U}dt\ , \tag{B.11}$$

and by a stress source, generally described as a double couple system of forces, becomes

$$I_{EN}\left(\mathbf{x}\right)=\int_0^T\mathcal{L}\left(\delta\mathbf{U},t\right)dt=-\int_0^T\nabla\cdot(\underline{\mathbf{t}}\cdot\delta\mathbf{U})\,dt\ . \tag{B.12}$$

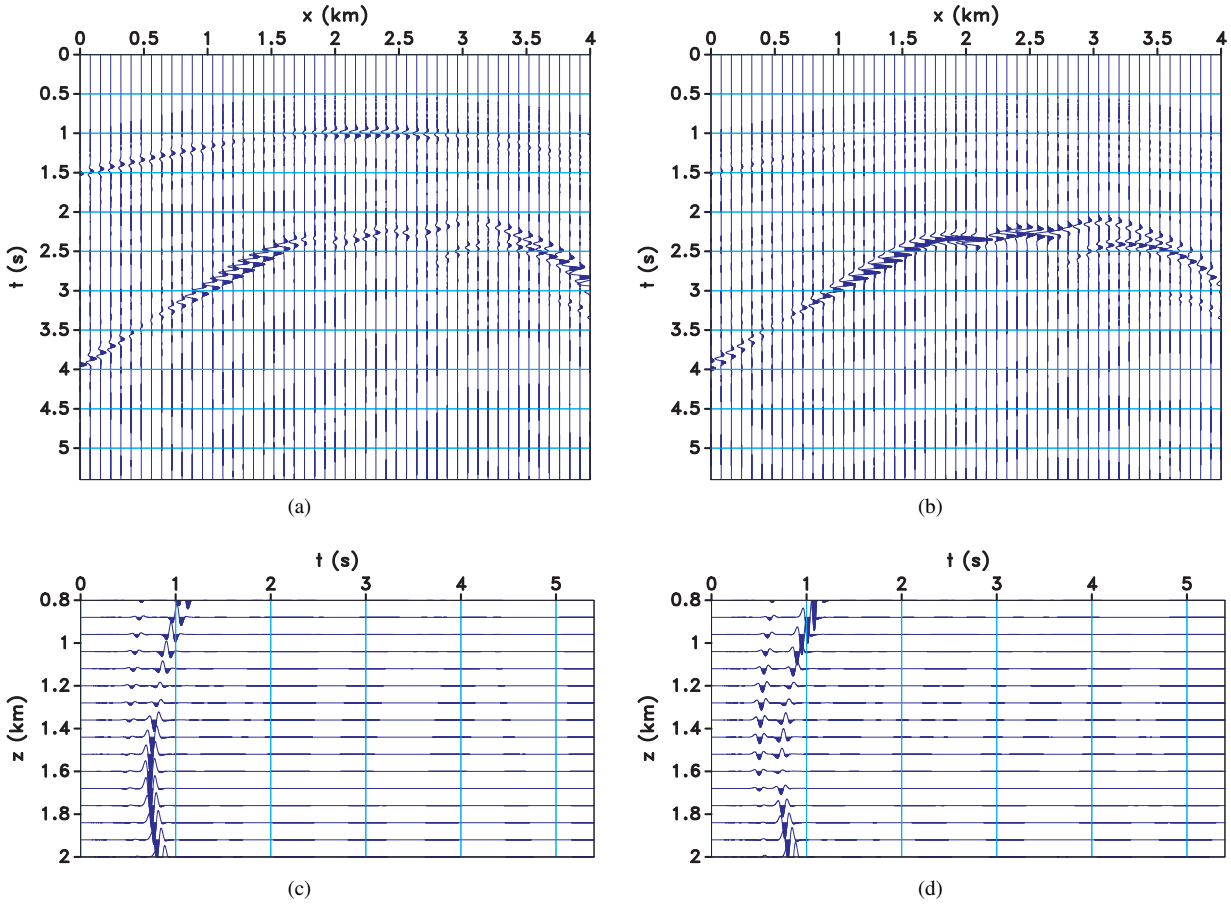


Figure 13. (a)(c) Vertical and (b)(d) horizontal displacement data acquired by the receivers at the surface and in the borehole, respectively.

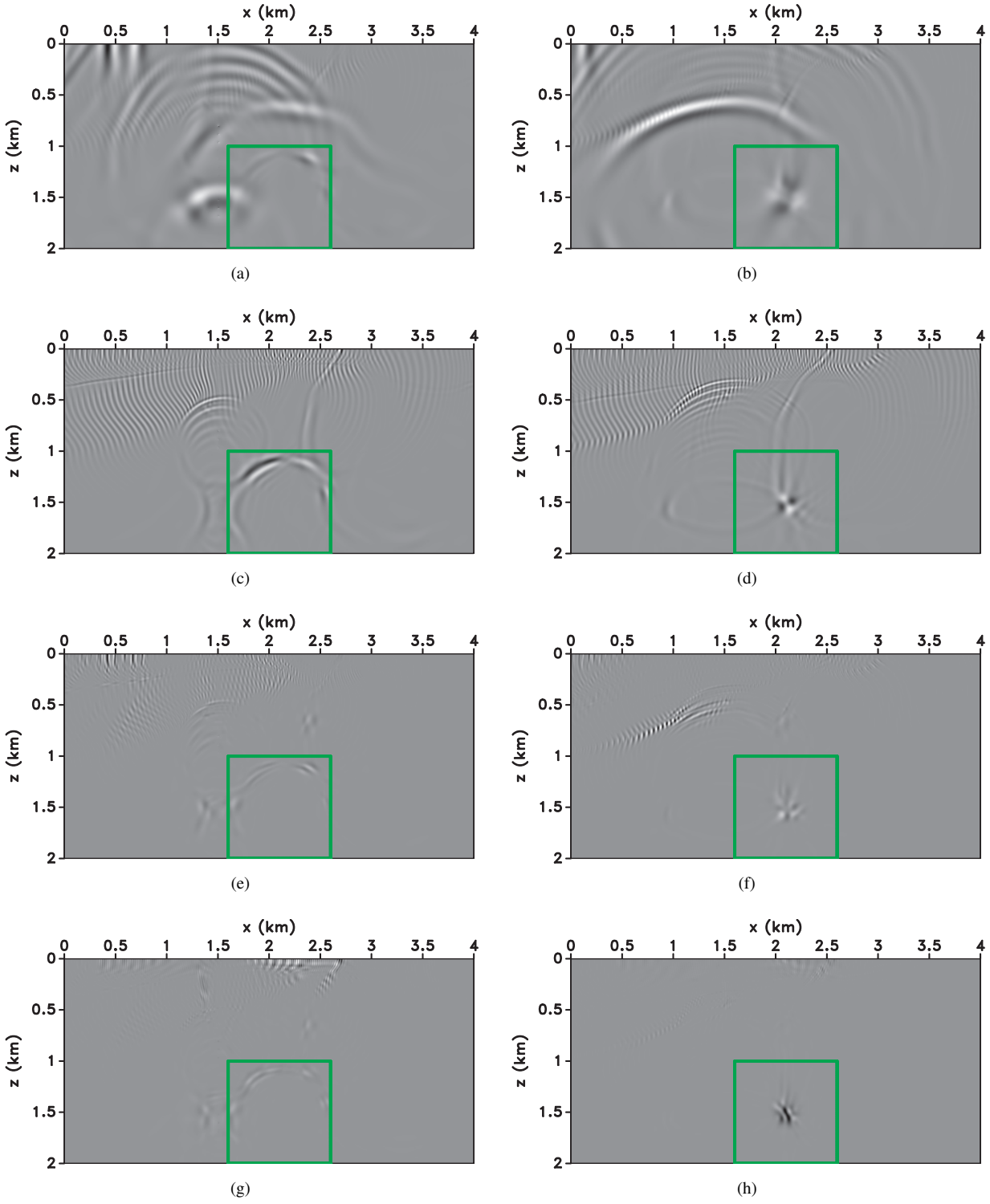


Figure 14. Wavefield snapshots for (a) (b) P- and (c)(d) S- waves, and for the (e)(f) PS and (g)(h) energy correlations at $t = 0.64$s and $t = 0.30$s, respectively. The source initial time is $t = 0.30$s.

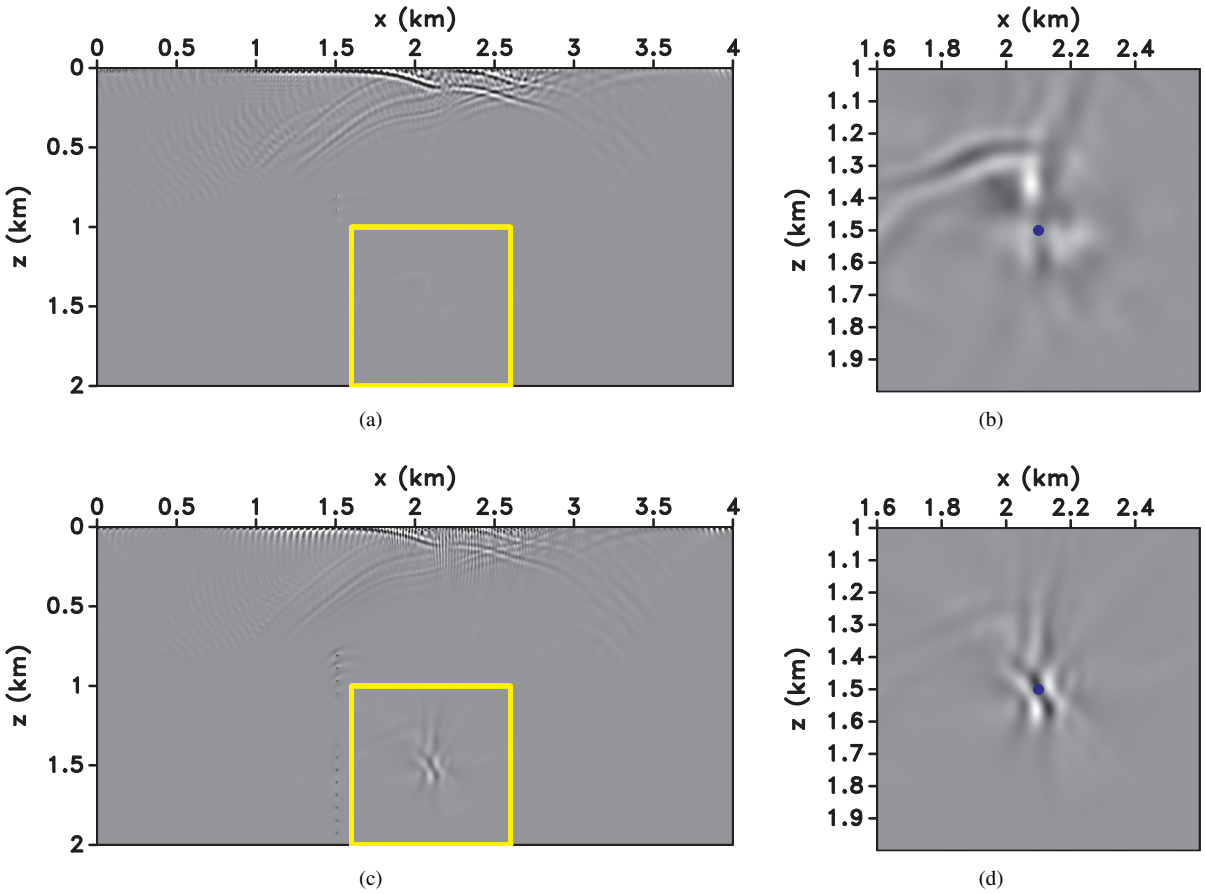


Figure 15. (a) PS and (c) energy images using the correct velocity, and both surface and borehole data. Zoomed (b) PS and (d) energy images.

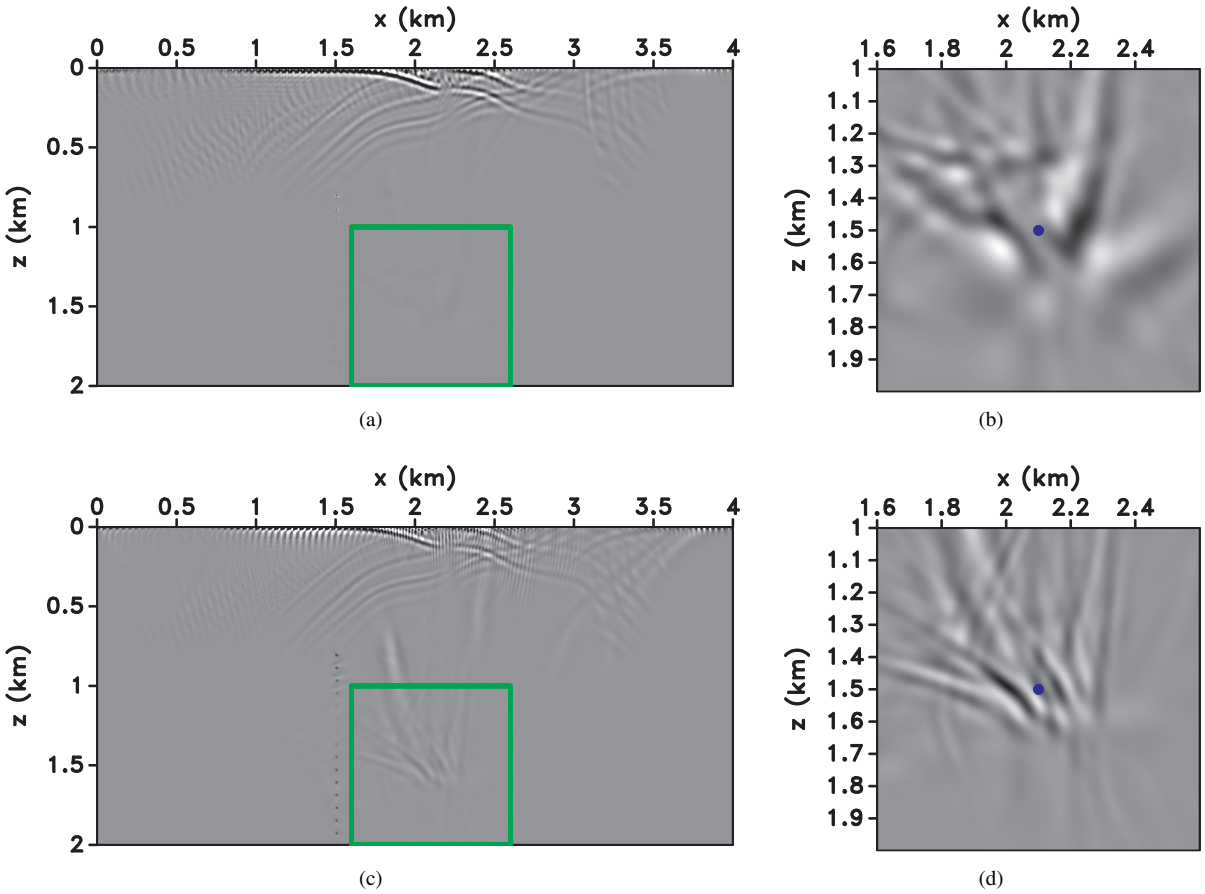


Figure 16. (a) PS and (c) energy images using the wrong velocity, and both surface and borehole data. Zoomed (b) PS and (d) energy images.